

# Calorimetric approach to paleo-detection of dark matter

S. Hedges and P. Huber\*

*Center for Neutrino Physics, Virginia Tech, Blacksburg, VA, USA*

(Dated: May 14, 2026)

We present the first paleo-detector dark matter sensitivity analysis based on a calorimetric readout, in which the number of stable lattice vacancies produced by each nuclear recoil is used as a per-event observable complementary to the track length. Using full-cascade SRIM simulations in olivine, we compute the expected sensitivity for a 100 g·1 Gyr exposure. We find that a vacancy-only readout reaches a sensitivity envelope very similar to that of state-of-the-art track-only analyses. The combination of the two observables provides an event-by-event proxy for  $|dE/dx|$  and hence for the recoiling nuclear species. Since the neutron-nucleus cross section is approximately flat in nuclear mass while the dark-matter–nucleus cross section scales as  $A^2$ , this discrimination suppresses the dominant neutron background by more than an order of magnitude at moderate dark matter masses. The combined-analysis sensitivity reaches spin-independent dark-matter–nucleon cross sections of order  $10^{-48}$  cm<sup>2</sup> at WIMP masses of a few tens of GeV, comparable to future direct detection experiments. A two-stage readout combining selective-plane illumination microscopy with scanning electron microscopy is identified as a path to making a 100 g-scale analysis plausible.

## I. INTRODUCTION

Persistent structural damage from nuclear interactions in solids has been used since the 1960s to date minerals [1]. The fission of uranium impurities in mica, apatite, and olivine produces tracks of order tens of micrometers in length which, once formed, remain stable for hundreds of millions of years and can be revealed by chemical etching and counted under an optical microscope [2, 3]. Thus minerals are natural detectors of nuclear events that have occurred in their volume during their lifetime. This has led to the idea that they can be used as detectors of rare events as well, in particular of speculative hitherto undiscovered new particles. First proposals looked for magnetic monopoles [4, 5] to be later followed by concepts for dark matter detection [6]. These methods are in aggregate referred to as *paleo-detectors*. Paleo-detection has seen a resurgence in interest [7–9]; in particular with the renewed interest in light dark-matter, that was dismissed prior to the LHC results. The basic idea is simple: a 100 g sample of 1 Gyr old mineral corresponds to an integrated exposure of 100 kt·yr, three orders of magnitude larger than currently planned liquid noble gas direct-detection experiments [10, 11]. Apart from the potentially large exposure, paleo-detection also allows us to learn about the radiation history of the sample in terms of atmospheric neutrinos [12], solar neutrinos [13], star formation [14] and cosmic rays [15, 16].

The dominant approach studied in the literature for extracting physics from this exposure has been to focus on the *track length* produced by each recoil [8, 9, 17]. In the initial phenomenological estimate, the track length left by a primary knock-on atom is approximated by integrating the inverse stopping power  $|dE/dx|^{-1}$  from zero to the recoil energy and depends on the recoiling species through  $|dE/dx|$ . More recently, fully simulated events have been used to determine the track length and with it the effect of fluctuations in track length has been studied as well [18].

The practical details of sub-micron track detection in gram-quantities of material have not been fully developed yet, but candidate technologies include scanning and transmission electron microscopy, small-angle X-ray scattering, helium-ion beam microscopy, atomic force microscopy, and others, see Ref. [9] for a review. These approaches yield strong sensitivity at moderate-to-high recoil energies but lose discriminating power at low recoil energy, where tracks become shorter than the resolution of the readout method.

The same underlying physics, however, provides an entirely complementary observable. Each recoil produces not only a track of finite length but also a population of stable lattice vacancies along that track with the total number scaling roughly with the deposited energy. Counting vacancies is therefore a calorimetric measurement, in much the same sense as the amount of silver in the photographic plates made by Röntgen with x-rays in 1895. In the context of paleo-detection, this observable has only recently become practically accessible at the single-event level, through fluorescence imaging of color centers in dielectric crystals using selective-plane illumination microscopy (SPIM) [19–21]: in many materials, vacancies form optically active color centers that fluoresce. That is, light of a specific wavelength causes each color center to emit light. Usually the excitation and emission wavelengths differ at finite temperature due to the Stokes shift. The emitted fluorescence light can be localized to within about 1/2 of its wavelength (neglecting

---

\* pahuber@vt.edu

details of the microscope optics). We will refer to a paleo-detector readout based on counting individual color centers as a “calorimetric” readout, in contrast to the “track-length” readouts that have dominated the literature so far. This paper is written in the context of the SPIM technology but the general findings likely apply to other calorimetric readout modalities.

The complementarity of tracking and calorimetric readouts has long been exploited in collider experiments. The general-purpose detectors at the LHC, CMS and ATLAS [22, 23], instrument both a high-resolution tracker that preserves the trajectories of charged particles and segmented calorimeters that absorb the particles and measure their total deposited energy. The two readouts give complementary information — topology and momentum on the one hand, total energy on the other — and combining them is essential for particle identification. The track-length and vacancy-count readouts of a paleo-detector are the analogues, at the molecular scale, of the tracker and the calorimeter at the collider scale, and the same logic motivates studying their combination here.

In this paper we present the first paleo-detector dark matter sensitivity analysis based on a calorimetric readout. We perform full-cascade SRIM simulations [24, 25] of the dominant signal and background channels in olivine and extract both track length and vacancy count event-by-event. We have chosen olivine since it is considered a good candidate from a geological point of view and it has been widely used in the paleo-detector literature, allowing for comparisons with existing results. We propagate the readout-specific parameters like light yield per vacancy, camera noise, and intrinsic defect concentration, through to the dark matter sensitivity. We find that a vacancy-based analysis alone reaches a sensitivity envelope very similar to state-of-the-art track-based analyses. More importantly, the combination of the two observables provides an event-by-event measure of the average  $|dE/dx|$  along the track, which acts as a discriminator of the recoiling nuclear species: since the neutron-nucleus cross section is approximately constant in nuclear mass while the dark-matter–nucleus cross section scales as  $A^2$ , this discrimination suppresses neutron backgrounds by more than an order of magnitude at moderate dark matter masses. The resulting combined-analysis sensitivity for 100 g of 1 Gyr old olivine reaches spin-independent dark-matter–nucleon cross sections in the  $10^{-48}$  cm<sup>2</sup> range at WIMP masses of a few tens of GeV, comparable to future liquid noble gas detectors. We further note that, even at the boundary of the neutrino fog [26, 27], paleo-detector experiments would still record  $10^3$ – $10^5$  dark-matter events — the limitation in this regime is systematic, not statistical.

The remainder of this paper is organized as follows. In section II we describe how track length and vacancy count are extracted from SRIM simulations and discuss the relative merits of the “fast” and “full cascade” simulation modes. In section III we define the target, exposure, signal model, and background model used throughout the analysis. We then present sensitivity results in section IV, comparing track-only and vacancy-only analyses, examining the impact of intrinsic defects, demonstrating the species-discrimination power of the (track length, vacancy count) plane, and presenting the combined-analysis sensitivity. Section V discusses the implications for the neutrino and neutron fog. We comment on practical large-mass readout in section VI and conclude in section VII.

## II. TRACKS VERSUS VACANCIES

The premise of paleo-detection is that persistent changes to the crystal structure encode information about the underlying particle interaction. A charged particle traversing a solid loses energy through three distinct channels: ionization, elastic lattice deformations, and inelastic lattice deformations. Neutral particles such as neutrinos, neutrons, and dark matter candidates first transfer their energy to a charged primary knock-on atom (PKA), which then deposits it through the same channels. For our purposes the relevant quantity is the inelastic deformation of the lattice, which produces the persistent vacancy population that constitutes the calorimetric signal. The other two channels must nevertheless be modeled correctly, since they govern the path along which vacancies are produced as well as energy loss between collision sites, and hence the track length.

The standard tool used in the paleo-detection community for these calculations is SRIM [24]. SRIM is a binary-collision Monte Carlo code that propagates energetic ions through matter, tracking the electronic and nuclear stopping along each trajectory; for each primary it returns the full sequence of secondary recoils, the deposited-energy spectrum, and the resulting populations of vacancies and interstitials. It has been the de facto standard for displacement-damage calculations in radiation physics for several decades. SRIM offers two distinct simulation modes, commonly referred to as “quick” (or “fast”) and “full cascade”. In quick mode, defects are generated according to the Kinchin-Pease approximation: the energy lost in any secondary collision is subtracted from the primary’s energy, and no secondary cascade is launched. In full cascade mode, by contrast, each secondary recoil generates its own cascade of subsequent recoils, and so on, until all knock-on atoms fall below the displacement threshold. In principle, full cascade should be the more physically faithful of the two, since the actual displacement physics is hierarchical. In practice, however, the two modes do not yield consistent results: a long-standing issue, characterized in detail in Ref. [25], is that full cascade mode does not correctly account for replacements, in which a vacancy is filled by a passing interstitial. As a result, full cascade overpredicts the number of stable vacancies by up to a factor of two relative to the quick mode,

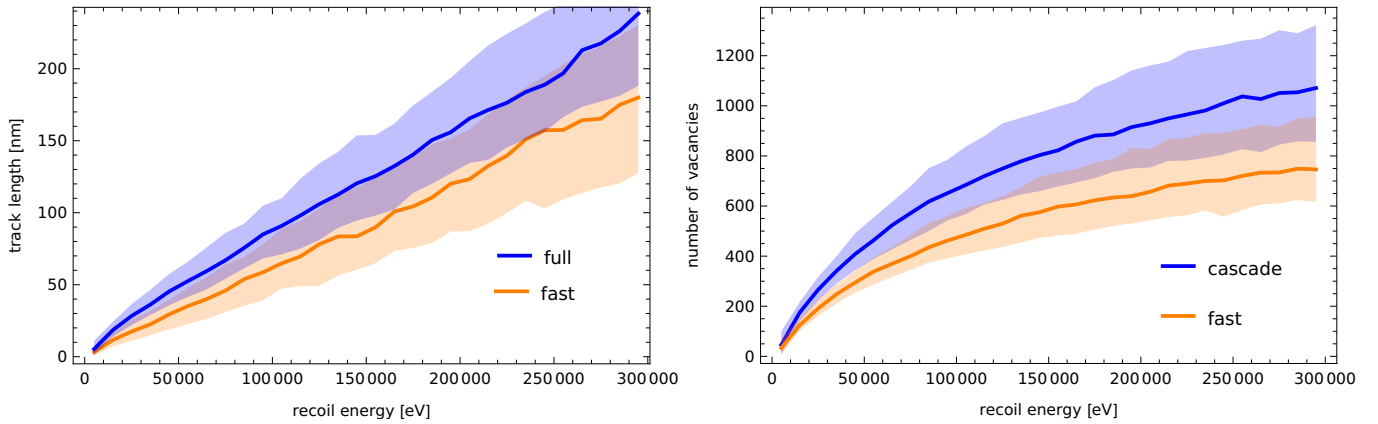


Figure 1. Distribution of track length (left panel) and number of vacancies (right panel) as a function of primary recoil energy, based on SRIM simulations in full cascade mode (blue) and quick mode (orange). The bands indicate the 68% quantile of the distributions. The data shown is for Fe primary knock-on atoms in olivine.

with somewhat smaller differences for the track length. This effect is illustrated in Fig. 1 for both observables, for iron primary recoils in olivine. We use full cascade simulations as our default throughout this work, since the resulting event topology is more realistic; we will return to the impact of the cascade-mode normalization uncertainty on dark matter sensitivity in section IV.

The SRIM simulations of olivine were conducted using the surface binding energy, lattice binding energy, and displacement energy from Refs. [28, 29] as compiled within Ref. [30]. The density of the olivine was assumed to be  $3.32 \text{ g cm}^{-3}$  [31]. Primary atoms were simulated with an energy of 1 MeV—a processing script tracked the energy of this primary as it collided with atoms in the lattice to generate a library of lower-energy primary damage tracks, all rotated to have an initial orientation in the same direction. The primary atom energies of interest for this study are all substantially lower than 1 MeV, allowing the primary to “burn in” and produce damage tracks spanning the 0–300 keV region of interest.

Near the vacancy production threshold, there is an energy-dependent probability that recoils produce zero vacancies. To compensate for this, vacancy production efficiency curves were generated by running mono-energetic primaries of each species from 0 eV up until the energy where an efficiency of 99.999% was achieved, using a 1 eV step size, typically on the order of a few hundred eV. Separate efficiency curves were generated for the full cascade and fast modes.

There is in general no simple one-to-one correspondence between vacancy formation and the type of color center created. For instance, in lithium fluoride, the same anion sublattice supports a family of related defects, like isolated F centers (anion vacancy  $+e^-$ ), di-vacancy  $F_2/M$  centers, tri-vacancy  $F_3/R$  centers, and their ionized counterparts  $F_2^+$  and  $F_3^+$ , whose absorption and emission bands span from the UV to the near-IR [32, 33]. Moreover, different types of irradiation populate the different types of color centers at a different rate [20]. Also in diamond we have many different types of color centers, many stemming from impurity vacancy combinations, *e.g.* the famous NV center, but also different vacancy centers like the GR1 and ND1 centers [34]. The sublattice the vacancy sits in also affects the type of color center formed, for instance in silicon carbide very different centers result from a missing carbon atom versus a missing silicon atom [35]. It stands to reason, that even for other readout modalities the relationship between vacancy formation and observable signature is far from trivial, *e.g.*, for x-ray-based methods the contrast is a strong function of the atomic number. This is not only a complication, but may provide signatures to disentangle the type of radiation that caused the signature as well as to aid in particle identification. This topic is rich and deserves further study but goes beyond the scope of the analysis presented here. Therefore, for simplicity we assume that vacancies of all atomic species contribute equally to the calorimetric signal and each vacancy gives rise to one color center.

The differences between the two simulation modes of SRIM go beyond an overall normalization. Figure 2 shows two simulated events of approximately 10 keV primary recoil energy: one in quick mode (filled disks) and one in full cascade mode (open circles). The PKA in both cases is iron, and the colors denote the atomic number of the recoiling atom along the cascade. The visual difference is striking: quick mode produces a roughly linear event with all damage along a single trajectory, whereas full cascade mode produces a much richer topology with off-axis branches and a more volume-filling event. This complicates the definition of a single track-length parameter for either type of simulation. Especially at lower recoil energies, events tend to become rounder, that is, their extents along the track direction and transverse to it become more and more comparable. At the lowest energies we have only a handful of vacancies that form more of a cloud than a linear track. Moreover, it is worth pointing out that even the concept of “track length resolution” is not an obvious one: when observing the etch pit of a fission track of  $\sim 20 \mu\text{m}$  length, the resolution

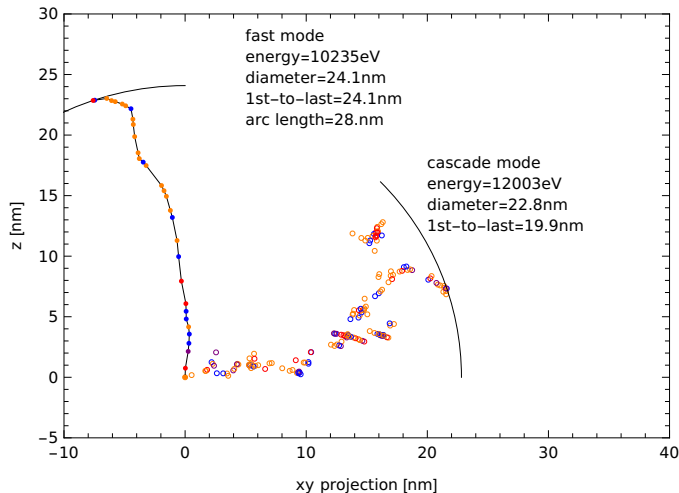


Figure 2. Projection into the  $xy$ -plane of two events simulated with SRIM at approximately 10 keV primary recoil energy. Filled disks show the result in quick mode, open circles show the result in full cascade mode. Each colored arc corresponds to one of the three track-length definitions discussed in the text: Euclidean first-to-last distance, arc length along the time-ordered cascade, and diameter (largest pairwise vacancy distance). Blue markers denote oxygen vacancies, orange markers denote magnesium vacancies, green markers denote silicon vacancies, and red markers denote iron vacancies.

required to see this event as a linear track is not the same as the track length. The optical microscopes employed in this type of analysis have an isotropic sub-micron resolution, *i.e.* much closer to the track width than to the length. X-ray techniques such as ptychography or tomography are more sensitive to the total volume of the disturbance of the lattice than the linear size of a feature. For very high resolution techniques like transmission electron microscopy, where every atom becomes visible, the distinction between track analysis and vacancy counting vanishes altogether. There is no clear dichotomy between reading out tracks and vacancy counts, nor is there a general definition of what type of resolution is actually required to see tracks of a certain size. These distinctions are conceptually very useful but hardly reflect experimental realities. With all these caveats in place, we nonetheless will use these simple categories going forward since they serve to illustrate the underlying concepts clearly.

A simple and natural length definition is the Euclidean distance between the first and last vacancy of the event. This works well in quick mode, where the cascade is essentially one-dimensional, but it is less well-defined in full cascade mode, where the transverse size of the event is not necessarily small compared to its length. A second option is the arc length obtained by connecting every vacancy in the time-ordered sequence; again, for full cascade events there is not one arc connecting all sub-cascades, and a choice would have to be made as to which sub-cascades to include. A close cousin of the arc length is the spline-fit technique introduced in Ref. [18], which suffers the same problem for events with sub-cascades. We also note that in real data the distinction of first and last event does not exist. A third definition that is not predicated on a linear event shape is given by the diameter of the event; the diameter is defined as the largest pairwise distance between any two vacancies. The diameter can be computed in  $\mathcal{O}(n \log n)$  time, where  $n$  is the number of vacancies, and is well-defined for any event topology. The three definitions are illustrated in Fig. 2 for both simulation modes. We find that the spread between definitions is generally smaller than the difference between full cascade and quick mode, and that the diameter tracks the other two definitions reasonably well in cases where they are unambiguous. Since the diameter applies uniformly to both simulation modes and to events of arbitrary topology, we adopt it as our default definition of track length throughout this paper. With these conventions in place, we now turn to the target, exposure, and background model used in the sensitivity analysis.

### III. TARGET, EXPOSURE, AND BACKGROUNDS

We adopt olivine,  $(\text{Mg, Fe})_2\text{SiO}_4$ , as the canonical target throughout this analysis, with the ratio of Mg/Fe being 4. Olivine is abundant in the Earth’s mantle and in many crustal rocks, has been extensively characterized in the fission-track-dating literature [2, 3], and contains a mixture of light and intermediate-mass nuclei, O, Mg, Si, and Fe, which proves convenient for distinguishing dark matter signals from neutron backgrounds, as we will discuss in section IV. Following Refs. [8, 9, 18] we take a benchmark exposure of 100 g of 1 Gyr old olivine, corresponding to an integrated 100 kt · yr, which is three orders of magnitude beyond the largest planned liquid noble gas dark matter

experiment [10, 11].

For the dark matter signal we assume a spin-independent contact interaction with nuclei. The WIMP-nucleus cross section is

$$\sigma_{\chi N} = \left( \frac{\mu_{\chi N}}{\mu_{\chi n}} \right)^2 A^2 \sigma_{\chi n}, \quad (1)$$

where  $\sigma_{\chi n}$  is the per-nucleon cross section,  $A$  is the target mass number, and  $\mu_{\chi N}$ ,  $\mu_{\chi n}$  are the WIMP-nucleus and WIMP-nucleon reduced masses. The coherent  $A^2$  enhancement is the basis of the species-discrimination argument of section IV C. The differential recoil rate per unit target mass is

$$\frac{dR}{dE_R} = \frac{\rho_\chi \sigma_{\chi n} A^2}{2 m_\chi \mu_{\chi n}^2} F^2(E_R) \eta(v_{\min}), \quad (2)$$

where  $\rho_\chi$  is the local dark matter density,  $m_\chi$  is the WIMP mass,  $F(E_R)$  is the nuclear form factor, and  $\eta(v_{\min}) = \int_{v_{\min}}^{\infty} f(v)/v dv$  is the mean inverse speed of the WIMP velocity distribution above the kinematic threshold  $v_{\min} = \sqrt{m_N E_R / 2 \mu_{\chi N}^2}$ . For the nuclear form factor we use the Helm parametrization [36, 37],

$$F(q) = \frac{3 j_1(q r_n)}{q r_n} \exp\left(-\frac{1}{2}(q s)^2\right), \quad (3)$$

with momentum transfer  $q = \sqrt{2 m_N E_R}$ , nuclear radius  $r_n^2 = c^2 + \frac{7}{3} \pi^2 a^2 - 5 s^2$ , and parameters  $c = 1.23 A^{1/3} - 0.60$  fm,  $a = 0.52$  fm, and surface thickness  $s = 0.9$  fm as given in Ref. [37].  $j_1$  is the order-1 spherical Bessel function of the first kind. For the WIMP velocity distribution we adopt the standard truncated Maxwellian with circular speed  $v_0 = 220$  km/s, local escape speed  $v_{\text{esc}} = 544$  km/s [38], average Earth speed  $v_E = 232$  km/s, and local dark matter density  $\rho_\chi = 0.3$  GeV/cm<sup>3</sup> [39], in agreement with Ref. [18]. The recoil energy spectrum from Eq. 2 is converted into a distribution in the (track length, vacancy count) plane through the SRIM simulation pipeline of section II, where each PKA at a given recoil energy is sampled from the corresponding cascade-by-cascade SRIM output.

Backgrounds fall into two distinct classes: those arising from the host mineral, and those arising from the imaging readout itself. The first class is dominated by neutrons produced through spontaneous fission of <sup>238</sup>U trace impurities and through  $(\alpha, n)$  reactions on light nuclei from  $\alpha$ -emitters in the U and Th decay chains. We use the *paleo-spec* framework [8, 17] for the neutron recoil spectrum and propagate it through SRIM in the same way as the signal. The <sup>238</sup>U concentration is the only normalization parameter for the neutron background; we adopt 0.1 ppb as our canonical value, with a 1% systematic uncertainty consistent with current rock-chemistry analyses. The  $\alpha$ -decay of <sup>238</sup>U into <sup>234</sup>Th produces a recoil nucleus of 72 keV energy resulting in a damage track in the  $\sim 30$  nm range. We include it as an additional, well-localized background class. Note, that we assume that all minerals have been so deep underground, at depths of  $\sim 5,000$  m or more, that direct muon-induced interactions can be neglected [8].

In addition to neutrons, coherent elastic neutrino-nucleus scattering generates an irreducible background from atmospheric neutrinos and from solar, diffuse, and galactic supernova neutrinos accumulated over the exposure period. Solar neutrinos contribute at low recoil energy through the pp, <sup>7</sup>Be, pep, <sup>13</sup>N, <sup>15</sup>O, <sup>17</sup>F, <sup>8</sup>B, and hep components; the diffuse supernova neutrino background (DSNB) and the galactic supernova neutrino background (GSNB), the latter representing  $\sim 1$  Gyr of accumulated galactic core-collapse neutrinos, contribute at intermediate energies; atmospheric neutrinos contribute at the highest recoil energies, where they are most relevant for high-mass dark matter searches. We use the standard fluxes and cross sections as summarized in Ref. [18] and take the numerical values from the *paleo-spec* framework [8, 17].

The second background class is specific to the calorimetric readout and proposed fluorescence microscopy method. In fluorescence spectroscopy the detectability of a given color center comes down to the light collection system and the camera noise. Without going into any technical details we can specify the number of photo-electrons (p.e.) that can be detected on average per color center, which we vary between 1 and 10 p.e. For the camera noise we use the specification of the Hamamatsu Orca Quest 2.0 camera, that yields 0.3 p.e. of noise per pixel. In addition, naturally occurring lattice defects in olivine produce a population of optically active color centers that are indistinguishable from radiation-induced single vacancies. We treat the intrinsic-defect concentration as a free parameter and study its impact on sensitivity in section IV; we adopt 1 ppb as the canonical value.

Figure 3 shows the resulting per-bin event counts in the track length (left panel) and vacancy count (right panel) for the dark matter signal and each background class, computed for the 100 g  $\cdot$  1 Gyr benchmark exposure. The solid and dashed curves correspond to full cascade and quick simulation modes, respectively, illustrating the per-class normalization differences discussed in section II. Several features are worth noting. Neutrons from <sup>238</sup>U fission dominate the rate at almost all track lengths and vacancy counts, with the exception of the lowest-recoil-energy bins

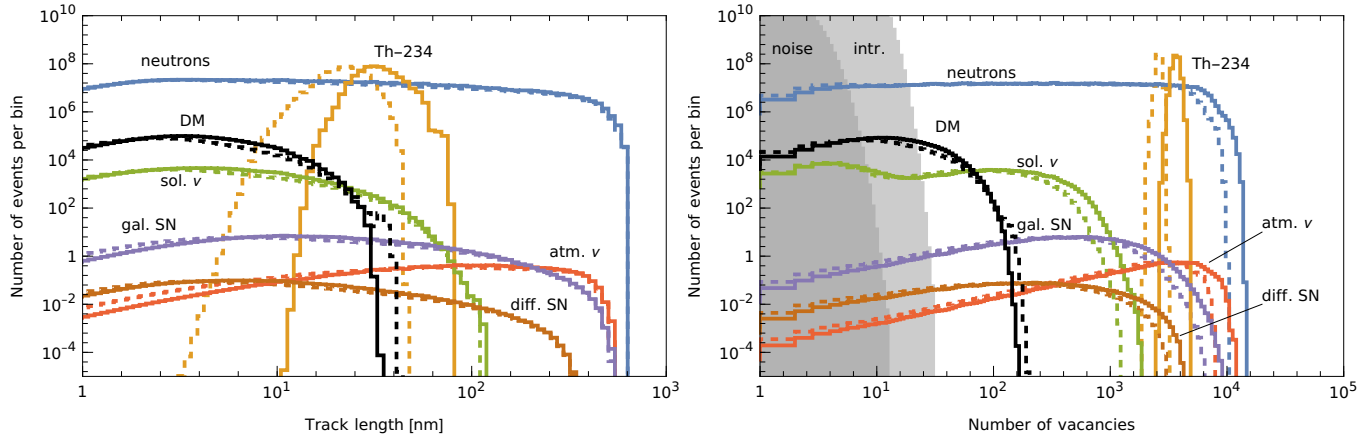


Figure 3. Track length (left panel) and vacancy count (right panel) distributions for the dark matter signal at  $m_\chi = 5 \text{ GeV}$  and  $\sigma = 10^{-45} \text{ cm}^2$ , and for each background class, for the  $100 \text{ g} \cdot 1 \text{ Gyr}$  olivine benchmark. Solid curves correspond to full cascade simulations, dashed curves to quick-mode simulations. The right panel assumes a per-vacancy light yield of 10 photo-electrons. The dark-gray shaded region indicates the camera noise floor; the light-gray shaded region indicates the contribution from 1 ppb of intrinsic vacancy defects.

where solar neutrinos take over. The daughter of the  $^{238}\text{U}$   $\alpha$ -decay,  $^{234}\text{Th}$  produces a sharp, narrow peak in track length around  $\sim 30 \text{ nm}$ . The dark matter signal shape overlaps significantly with all backgrounds in either projection considered separately: a fact that motivates the combined analysis of section IV C. The right panel additionally indicates the calorimetric-readout backgrounds: the camera noise floor at the lowest photo-electron counts (dark-gray shaded region) and the contribution from 1 ppb of intrinsic vacancy defects (light-gray shaded region).

Table I summarizes the systematic uncertainties used in the sensitivity analysis taken from Ref. [18]. The neutrino fluxes are quoted as fractional uncertainties on their predicted spectra: the solar flux is constrained at the 14% level by direct measurements, while the DSNB, GSNB, and atmospheric fluxes are treated as 100% uncertain since they are at most weakly constrained. The  $^{238}\text{U}$  concentration in any specific olivine sample can be measured to 1% by destructive chemical analysis, the mineral age can be determined to  $\sim 5\%$  by independent geochronology, and the mineral mass is known to better than 0.01%. We note, that in practice these systematic uncertainties play little role in the analysis since the shapes of the distributions, in both the track-length and vacancy-count parameters, distinguish the background from the signal. This, of course, is all based on simulation, and if in reality the backgrounds are found to be highly structured this finding will need to be revisited.

Parameter $n_i$	Error $\sigma_i$
$\nu_{\text{solar}}$ flux	14%
$\nu_{\text{DSNB}}$ flux	100%
$\nu_{\text{GSNB}}$ flux	100%
$\nu_{\text{ATM}}$ flux	100%
$^{238}\text{U}$ concentration	1%
Mineral age $t$	5%
Mineral mass $m_{\text{olivine}}$	0.01%

Table I. Systematic uncertainties used in the sensitivity analysis, following Ref. [18]. Neutrino fluxes are quoted as fractional uncertainties on the predicted spectra. The mineral parameters are quoted as fractional uncertainties on independently-measurable quantities of the host olivine sample.

#### IV. DARK MATTER SENSITIVITY

We compute 90% C.L. exclusion limits on the spin-independent dark matter–nucleon cross section using a binned Gaussian likelihood<sup>1</sup> profiled over the nuisance parameters of Tab. I, following the procedure of Ref. [18]. We present

<sup>1</sup> A Gaussian likelihood is numerically more efficient and the event counts even at the limit are in the 1,000s, hence the underlying Poisson statistics is effectively approximated by a Gaussian one. We use 1 degree of freedom for determining the critical value of the test statistic

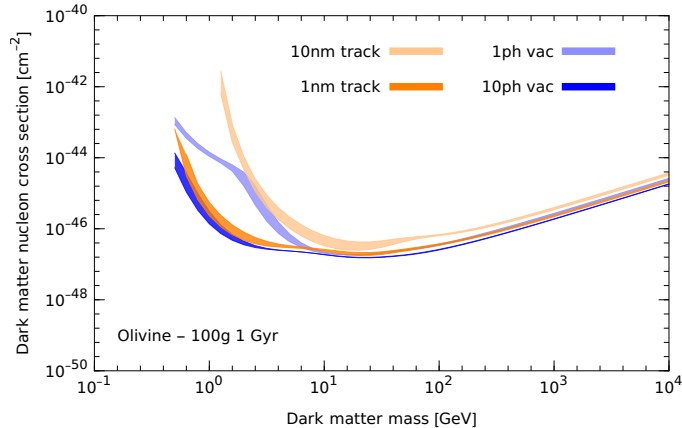


Figure 4. 90% C.L. sensitivity limits on the spin-independent dark matter–nucleon cross section as a function of dark matter mass, for 100 g of 1 Gyr old olivine. Track-only analyses are shown for track-length resolutions of 1 nm and 10 nm; vacancy-only analyses are shown for per-vacancy light yields of 1 and 10 photo-electrons. The bands span full cascade simulations (lower edge) and quick simulations (upper edge).

the results in four steps that progressively build up the calorimetric analysis: track-only versus vacancy-only sensitivity, the impact of intrinsic-defect contamination, the species-discrimination power of the joint observable, and the combined-analysis sensitivity. For the track length we use 100 bins evenly spaced on a logarithmic scale from 1/2 of the track length resolution up to 1000 nm. We do apply a resolution function, taken to be a Gaussian smearing in  $\log L$  with width set by the assumed track-length resolution, as described in Ref. [18]. For the number of vacancies we use 166 bins, where we have bins of width 1 from 1 to 16 and then uniformly on a logarithmic scale up to 500,000 vacancies. We use a Poisson distribution to model the count rate uncertainty on the photo-electrons. For the combined analysis we use the same bin sizes but in a two-dimensional grid where events that fall below the track resolution limit are put into an overflow bin, *i.e.* events in this bin are only binned in vacancy number but not in track length.

### A. Track-only and vacancy-only readout

Figure 4 shows the 90% C.L. sensitivity envelope obtained when only one of the two observables is used. For the track-only analysis we consider track-length resolutions of 1 nm and 10 nm, bracketing what current and near-future readout techniques are expected to achieve [9]. For the vacancy-only analysis we vary the per-vacancy light yield between 1 and 10 photo-electrons, bracketing the range expected for existing and improved imaging readouts [19, 20]. The bands on each curve indicate the spread between full cascade and quick simulation modes, which is largest at low dark matter mass and amounts to at most a factor of a few in the cross section.

The principal observation from Fig. 4 is that the vacancy-only and track-only analyses reach very similar sensitivities across the entire mass range. At dark matter masses above  $\sim 10$  GeV both readouts approach the  $10^{-47}$  cm<sup>2</sup> scale. The two readouts differ only in the low-mass tail, where the small number of vacancies per signal event makes the calorimetric channel slightly less sensitive than a high-resolution track-length readout. This near-equivalence is an interesting and important finding; it also highlights that the real performance of the readout technology will be the decisive factor for low-mass performance.

### B. Intrinsic-defect contamination

Naturally occurring lattice defects in olivine are an irreducible background specific to the calorimetric readout. To quantify their impact we vary the intrinsic-defect concentration over the range 0.01 to 1 ppb while holding all other parameters at their canonical values. The result is shown in Fig. 5.

We find that the high-mass sensitivity is essentially unaffected by intrinsic defects: signal events at high recoil energy produce hundreds of vacancies, far above the few-vacancy contamination floor expected even at the highest

---

which we assume to follow a  $\chi^2$ -distribution.

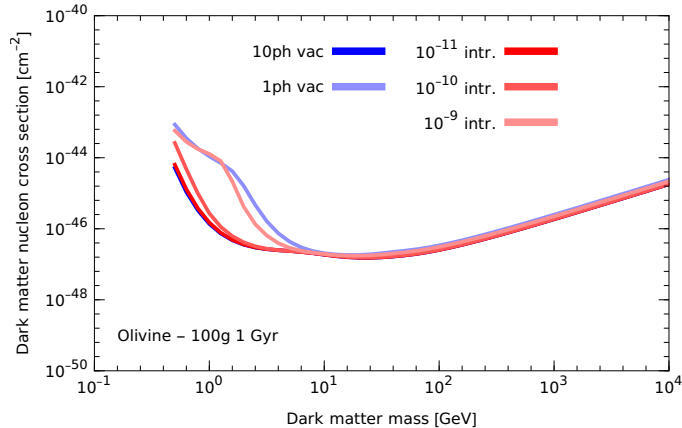


Figure 5. 90% C.L. sensitivity limits on the spin-independent dark matter–nucleon cross section as a function of dark matter mass, for 100 g of 1 Gyr old olivine. The vacancy-only sensitivity is shown for an assumed light yield of 10 photo-electrons per vacancy and intrinsic-defect concentrations of 0.01, 0.1, and 1 ppb (red, from darkest to lightest). For comparison, the defect-free results for 1 and 10 photo-electrons per vacancy are also shown (blue, light and dark).

defect concentrations considered here. The low-mass tail, however, is sensitive to the defect concentration. Above  $\sim 1$  ppb the calorimetric sensitivity to dark matter masses below  $\sim 5$  GeV degrades by an order of magnitude or more; below  $\sim 0.1$  ppb the impact is negligible. We therefore identify  $\sim 1$  ppb as the optical active defect concentration above which the low-mass calorimetric channel is significantly compromised, and as a benchmark for the required olivine purity in any practical implementation.

### C. Species discrimination in the (track length, vacancy count) plane

The marginal distributions of Fig. 3 obscure information that is preserved in the joint distribution. The neutron-nucleus cross section is approximately flat in nuclear mass, and so neutron-induced recoils populate all species in olivine roughly in proportion to their abundance. The spin-independent dark matter–nucleus cross section, by contrast, scales as  $A^2$  in the Helm form factor regime, and so dark matter recoils concentrate strongly on iron, the heaviest abundant nucleus in olivine. At a given recoil energy, heavier nuclei have lower velocity, so a larger fraction of their energy goes into nuclear rather than electronic stopping; their nuclear stopping power per unit length is also larger. The combined effect is that heavier PKAs produce shorter tracks and more vacancies. The pair (track length, vacancy count) thus acts as a per-event proxy for the specific energy loss  $|dE/dx|$  and consequently for the recoiling species.

This expectation is borne out in Fig. 6, which shows the joint two-dimensional distribution of track length and vacancy count for the neutron background and for a 500 GeV mass dark matter signal. The two populations overlap in either projection but separate clearly in the joint plane: the dark matter signal occupies the region of higher vacancy count and shorter tracks, corresponding to recoils on iron, while the neutron background extends to the lower-vacancy-count, longer-track region populated by recoils on oxygen, magnesium, and silicon. The same separation persists at other masses but practically becomes less relevant for low recoil energies since here the signal in any case is just a handful of vacancies and a track length can hardly be defined. This species-discrimination power is the conceptual basis for the calorimetric advantage: it suppresses the dominant neutron background at the per-event level, without any reliance on its absolute normalization. Whether the same plane can be used to discriminate between different dark matter–nucleon couplings, beyond the spin-independent contact interaction considered here, is an interesting question that we leave for future work. It also is worth noting that minerals that are composed of elements covering a large range in atomic masses will exhibit this effect to a larger degree than minerals that are chemically pure, *e.g.* diamond. Olivine spans roughly a range of 3.5 in atomic masses, but for instance zircon spans a range of 5.7 and barite a range of 8.5; this adds a novel selection criterion for target minerals for paleo-detection. As mentioned in section II, in reality several species of color centers will be produced and likely can be distinguished spectroscopically, enhancing the particle identification. Also using track length as a single descriptor of the spatial morphology of the event is probably not the best way to characterize the information contained in the event and other more complex measures of morphology could be employed.

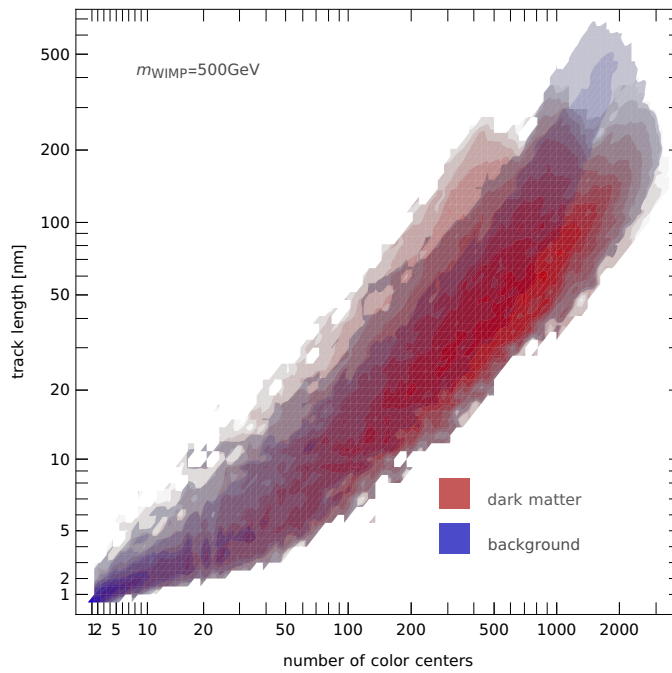


Figure 6. Joint two-dimensional histograms in the (vacancy count, track length) plane for the neutron background (blue) and a dark matter signal at  $m_{\text{WIMP}} = 500 \text{ GeV}$  (red), for the  $100 \text{ g} \cdot 1 \text{ Gyr}$  olivine benchmark. Color intensity represents the per-bin event density of each distribution on a logarithmic scale, with darker shading indicating higher density.

#### D. Combined analysis

Figure 7 shows the combined-analysis sensitivity (green curve), computed using the joint likelihood in the (track length, vacancy count) plane, alongside the track-only and vacancy-only envelopes from Fig. 4. Since the analysis is based on the full two-dimensional likelihood no cuts are used to reject neutron backgrounds. The combined analysis reaches  $\sigma \sim 10^{-48} \text{ cm}^2$  at  $m_\chi$  of a few tens of GeV, roughly an order of magnitude below either single-observable analysis at the optimum mass. The improvement comes from the species-discrimination argument of section IV C: the joint fit suppresses neutron contamination at the per-event level rather than relying solely on its absolute normalization.

The dark-gray and light-gray shaded regions in Fig. 7 indicate the current and projected reach of liquid noble gas dark matter experiments [10, 11, 40]. The combined-analysis envelope reaches sensitivity comparable to the projected reach of XLZD-class detectors at moderate dark matter masses, with somewhat better low-mass reach where the lower energy threshold of crystal targets and the long exposure period of paleo-detectors are both decisive advantages. At high mass,  $m_\chi \gtrsim 1 \text{ TeV}$ , the combined analysis remains comparable to the projected liquid noble gas reach. The achievable sensitivity is ultimately set by the irreducible neutrino background, which we discuss in the next section.

#### V. THE NEUTRINO AND NEUTRON FOG

The achievable sensitivity of any rare-event search is ultimately limited by irreducible backgrounds, which for direct dark matter detection usually means coherent elastic neutrino-nucleus scattering. The corresponding sensitivity floor is conventionally referred to as the *neutrino fog* [26, 27]; for paleo-detectors the long exposure period also makes neutron backgrounds irreducible, and we will refer to the joint structure as the *neutrino and neutron fog*. Following Ref. [27] we quantify the depth of the fog by the slope of the discovery cross section with exposure,

$$n = \left( \frac{d \ln \sigma}{d \ln N} \right)^{-1}. \quad (4)$$

For a background-free experiment  $n = 1$ , corresponding to  $\sigma_{\text{disc}} \propto 1/N$ . For an experiment dominated by an irreducible background of perfectly known normalization, Asimov statistics give  $n = 2$ . In the limit where systematic

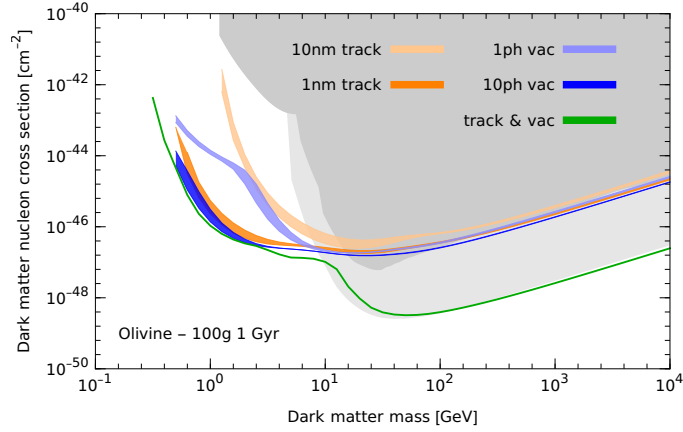


Figure 7. 90% C.L. sensitivity limits on the spin-independent dark matter–nucleon cross section as a function of dark matter mass, for 100 g of 1 Gyr old olivine. The green curve shows the combined analysis using the joint (track length, vacancy count) likelihood; the orange and blue curves show the track-only and vacancy-only envelopes from Fig. 4. The dark-gray and light-gray shaded regions indicate the current and projected reach of liquid noble gas direct-detection experiments. All results use full cascade simulations.

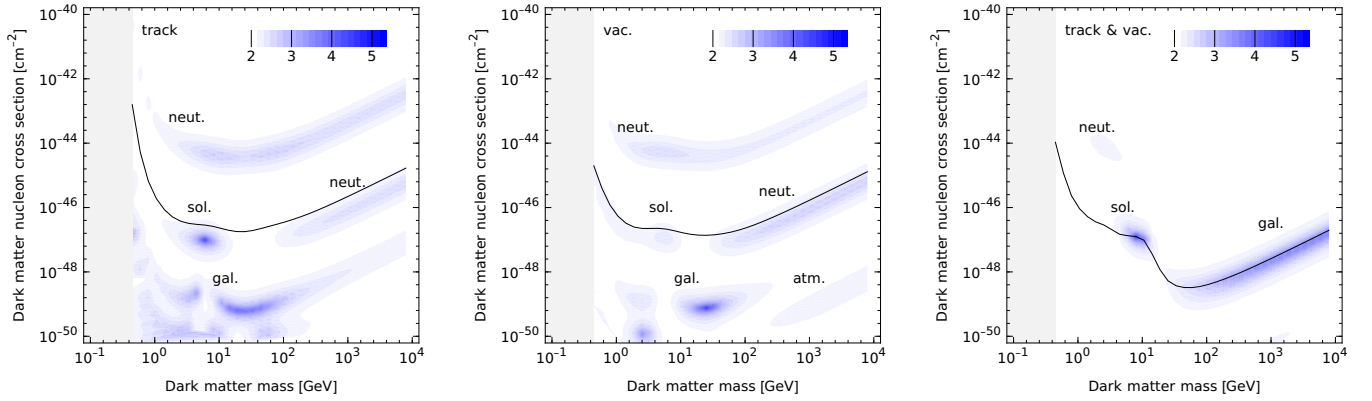


Figure 8. Neutrino and neutron fog for the 100 g · 1 Gyr olivine benchmark, for the track-only (left panel), vacancy-only (middle panel), and combined (right panel) analyses. Colored regions show contours of the fog parameter  $n = (d \ln \sigma / d \ln N)^{-1}$  (Eq. 4), and the black lines mark the corresponding 90% C.L. sensitivities. The labels identify the dominant background behind each island: neutrons (“neut.”), solar neutrinos (“sol.”), galactic supernova neutrinos (“gal.”), atmospheric neutrinos (“atm.”), and the diffuse supernova neutrino background (“diff.”). The transition to  $n = 1$  for cross sections in the  $10^{-42}$ – $10^{-40}$   $\text{cm}^2$  range corresponds to the background-free regime where statistical scaling becomes linear in exposure.

uncertainties on the background dominate over statistical fluctuations,  $n \rightarrow \infty$  and additional exposure brings no further gain. The conventional definition of the fog boundary is the contour  $n = 2$ .

Figure 8 shows the fog structure for our 100 g · 1 Gyr olivine benchmark, in three configurations: a track-only analysis (left panel), a vacancy-only analysis (middle panel), and the combined analysis of section IV (right panel). In each panel the colored regions are contours of  $n$  in the (dark matter mass, cross section) plane, and the black line is the corresponding 90% C.L. sensitivity. Several distinct islands are visible, each driven by a specific background: neutrons (“neut.”), solar neutrinos (“sol.”), galactic supernova neutrinos (“gal.”), atmospheric neutrinos (“atm.”), and the diffuse supernova neutrino background (“diff.”). The transition to  $n = 1$ , where the experiment becomes effectively background-free and the discovery cross section scales linearly with exposure, occurs at cross sections in the  $10^{-42}$  to  $10^{-40}$   $\text{cm}^2$  range and is not shown. Realistic paleo-detector targets lie well below this transition, so any practical search operates inside the fog, be it neutrons or neutrinos.

Comparing the three panels, the most striking feature is the recession of the fog when going from single-observable to combined analysis. The neutron-fog island, dominant in both single-observable panels, is largely suppressed in the

combined panel, reflecting the species-discrimination power discussed in section IV C. The combined analysis pierces the floor at moderate dark matter masses, where the dominant background after combination is a much smaller neutrino contribution. At low and high masses the floor is instead set by neutrino backgrounds, from solar and atmospheric neutrinos respectively, and is essentially unchanged from the single-observable case — for the specific set of elements, atomic masses and neutron numbers the specific energy loss for neutrino-induced and dark matter-induced recoils is too similar to be resolved even with the combination of track length and vacancy count.

A further noteworthy feature is the absolute event count at the fog-implied limit. Where conventional direct detection experiments encounter the neutrino floor at expected signal counts of order tens of events, our 100 g · 1 Gyr olivine benchmark would record  $10^3$ – $10^5$  dark matter events at the same boundary, depending on mass. The limitation in this regime is therefore systematic rather than statistical. Many of the systematic uncertainties will come from the geological history of the sample.

## VI. PRACTICAL READOUT CONSIDERATIONS

The sensitivity benchmark assumed throughout this paper is 100 g of olivine, as a sample of that size contains about  $10^9$  events from neutron and neutrino interactions, the dominant contribution coming from neutron-induced recoils accumulated over the 1 Gyr exposure. Reading out this volume at the 1 nm resolution required for individual event reconstruction using the track length as a signature would generate a data volume of about 100 zettabytes ( $10^{23}$  Bytes), comparable to or exceeding that of the high-luminosity LHC at the detector level [41]. This indicates that a single-stage readout at nanometer resolution across the full 100 g sample would currently be very difficult, if not impossible, simply based on data volumes alone.

The key observation is that the high-resolution readout does not need to be applied to the entire sample volume; only to the small fraction occupied by candidate events. This motivates a two-stage approach. In the first stage, the entire sample is scanned at coarse, micron-scale resolution using selective-plane illumination microscopy [20, 21]. Recent measurements in the Huber lab have demonstrated SPIM imaging of LiF samples up to  $0.5 \text{ cm}^3$  in volume [42], indicated by the 2026 SPIM marker in Fig. 9. Regions in which the SPIM scan identifies one or more color centers are flagged as candidate events, and from Fig. 3 together with the optical resolution of the type of SPIM used for paleo-detection [20] we can infer that each event would be contained in a  $1 \mu\text{m}^3$  volume. Thus the total volume for the high-resolution scan is about  $10^9 \mu\text{m}^3 = 0.001 \text{ cm}^3$ . Given the density of olivine, the full volume is about  $30 \text{ cm}^3$ , thus only 1 part in 30,000 of the volume requires a high-resolution readout. In the second stage, only those flagged regions of interest are imaged at the nm-scale using scanning electron microscopy (SEM), which resolves individual color centers but at a much smaller per-volume rate. The first stage prefilters the volume; the second stage delivers the resolution.

Recent results in connectomics show that a petascale SEM analysis of  $\sim 1 \text{ mm}^3$  of human cortex is possible [43], generating  $\sim 1.4$  petabytes of imaging data and reconstructing  $\sim 150$  million synapses across 57,000 cells in a fully-automated pipeline. Modern multi-beam SEMs can image  $\text{mm}^3$ -sized regions at nanometer resolution. The time required is still significant; in this example 326 days of scanning were required [43], and the corresponding data rates have been demonstrated to be tractable. The high-resolution scan volume required for a 100 g paleo-detector readout is comparable to this, provided that the SPIM stage prefilters the sample efficiently. This simple argument of course does not address how to isolate the  $10^9$  ROIs within the 100 g sample and how to make them accessible for SEM. In the connectomics example the tissue was physically sliced into 30 nm-thick sections and each section was then scanned in full under the SEM, taking full advantage of modern multi-beam SEM technology. It does, however, show that raw scanning and data-handling capacity exists that is close to what is required for a full two-stage dual-readout of a 100 g sample.

Figure 9 sketches the relevant mass-versus-resolution landscape. The single-stage SPIM and SEM technologies span complementary regions of the (mass, resolution) plane: SPIM reaches gram-scale samples at micron resolution, SEM reaches milligram-scale samples at nanometer resolution. Diagonal lines in the figure indicate contours of constant data volume, with the band corresponding to high-luminosity LHC data rates [41] shown for reference. The two-stage approach (arrow) bridges the gap, reaching the 100 g benchmark of this paper at the resolution required for individual color-center localization. The data volumes involved are formidable but not unprecedented; the analysis pattern, a small number of high-resolution windows distributed across a much larger coarse-scan volume, is theoretically well-matched to automated pipelines. An actual working implementation for paleo-detection, however, remains to be developed.

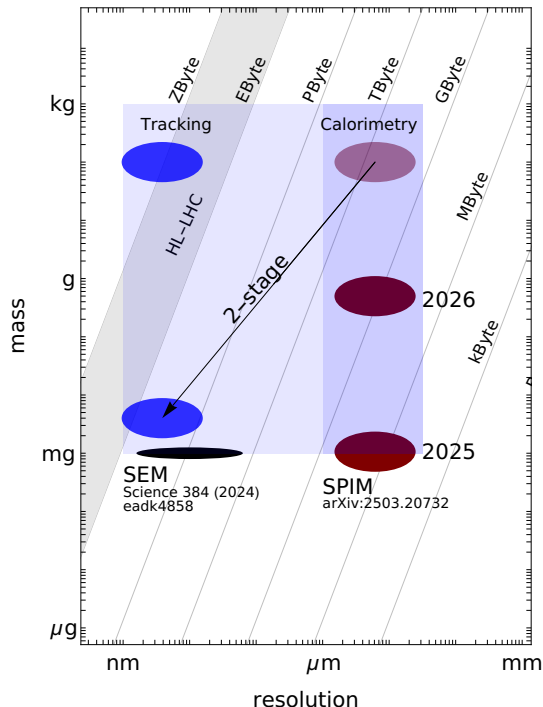


Figure 9. Mass-versus-resolution landscape for paleo-detector readout. SPIM (selective-plane illumination microscopy) reaches gram-scale samples at micron resolution; SEM (scanning electron microscopy) reaches milligram-scale samples at nanometer resolution. The two-stage approach (arrow) composes the two to reach the 100 g benchmark of this paper at nanometer resolution. Reference markers indicate current capabilities of SPIM [20] and SEM [43]; the 2026 SPIM marker corresponds to a recent  $0.5 \text{ cm}^3$  LiF measurement in the Huber lab [42]. Diagonal lines indicate constant data volumes, with the high-luminosity LHC band shown for comparison [41].

## VII. CONCLUSION

We have presented the first paleo-detector dark matter sensitivity analysis based on a calorimetric readout, in which the number of stable lattice vacancies produced by each nuclear recoil is used as a per-event observable complementary to the track length. Using full-cascade SRIM simulations of the dominant signal and background channels in olivine, neutrons from  $^{238}\text{U}$  fission,  $^{234}\text{Th}$   $\alpha$ -decay recoil, atmospheric and solar neutrinos, and diffuse and galactic supernova neutrinos, we have computed the expected sensitivity for a  $100 \text{ g} \cdot 1 \text{ Gyr}$  exposure. New parameters introduced by the calorimetric readout like per-vacancy light yield, camera noise, and intrinsic-defect concentration have been studied. We find that the differences between full cascade and quick SRIM modes lead to at most a factor-of-a-few uncertainty in the cross-section limits and do not qualitatively change any of our conclusions. For a real experiment these discrepancies will need to be resolved, of course, and any simulation will need to be calibrated against real data.

The principal finding is that, for the benchmark exposure considered here, a vacancy-only readout reaches a sensitivity envelope very similar to that of state-of-the-art track-only analyses. More importantly, the combination of the two observables provides an event-by-event proxy for  $|dE/dx|$  and hence for the recoiling nuclear species. Because the neutron-nucleus cross section is approximately flat in  $A$  while the dark matter-nucleus cross section scales as  $A^2$ , this discrimination suppresses the dominant neutron background by more than an order of magnitude at moderate dark matter masses. The combined-analysis sensitivity is comparable to the projected reach of XLZD-class liquid noble gas detectors, with somewhat better low-mass reach. Even at the boundary of the neutrino and neutron fog, paleo-detector experiments would record  $10^3$ – $10^5$  dark matter events: the limitation in this regime will be systematics, mostly stemming from the geological history of the sample.

Reading out a 100 g olivine sample at the required resolution is a formidable task. A two-stage approach combining selective-plane illumination microscopy with scanning electron microscopy on flagged regions of interest brings the data volumes to a level comparable with petascale connectomics workflows. Recent progress in connectomics gives rise to the hope that a two-stage readout scheme may be approaching feasibility. Importantly, readout of 100 g of material is currently feasible using calorimetry alone; the resulting sensitivity to dark matter of a purely calorimetric

readout is comparable to that of a track-based paleo-detector. A dual calorimetric/track paleo-detector offers a complementary path to the conventional liquid noble gas approach, achieving competitive dark matter sensitivity through long exposure rather than large instantaneous mass.

## ACKNOWLEDGMENTS

This work was supported by the U.S. Department of Energy National Nuclear Security Administration’s Enabling Capabilities in Technology (Tech) Consortium under award number DE-NA0004197. It was also supported by the U.S. Department of Energy Office of Science under award number DE-SC0020262. It was also supported by a National Science Foundation Growing Convergence Research award number 2428507.

- 
- [1] P. B. Price and R. M. Walker, “Fossil tracks of charged particles in mica and the age of minerals,” *Journal of Geophysical Research* **68**, 4847–4862 (1963).
  - [2] G. A. Wagner and P. Van den haute, *Fission Track Dating* (Ferdinand Enke Verlag, Stuttgart, 1992).
  - [3] A. J. W. Gleadow, D. X. Belton, B. P. Kohn, and R. W. Brown, “Fission track dating of phosphate minerals and the thermochronology of apatite,” *Reviews in Mineralogy and Geochemistry* **48**, 579–630 (2002).
  - [4] R. L. Fleischer, Jr. Hart, H. R., I. S. Jacobs, P. B. Price, W. M. Schwarz, and F. Aumento, “Search for magnetic monopoles in deep ocean deposits,” *Physical Review* **184**, 1393–1397 (1969).
  - [5] P. B. Price and M. H. Salamon, “Search for supermassive magnetic monopoles using mica crystals,” *Physical Review Letters* **56**, 1226–1229 (1986).
  - [6] D. P. Snowden-Ifft, M. K. Y. Chan, and R. Frenkel, “Compositional dependence of the formation of nuclear tracks in muscovite mica,” *Phys. Rev. Lett.* **74**, 4133–4136 (1995).
  - [7] Andrzej K. Drukier, Sebastian Baum, Katherine Freese, Maciej Górski, and Patrick Stengel, “Paleo-detectors: Searching for Dark Matter with Ancient Minerals,” *Phys. Rev. D* **99**, 043014 (2019), arXiv:1811.06844 [astro-ph.CO].
  - [8] Sebastian Baum, Andrzej K. Drukier, Katherine Freese, Maciej Górski, and Patrick Stengel, “Searching for Dark Matter with Paleo-Detectors,” *Phys. Lett. B* **803**, 135325 (2020), arXiv:1806.05991 [astro-ph.CO].
  - [9] Sebastian Baum *et al.*, “Mineral detection of neutrinos and dark matter. A whitepaper,” *Phys. Dark Univ.* **41**, 101245 (2023), arXiv:2301.07118 [astro-ph.IM].
  - [10] J. Aalbers *et al.* (DARWIN), “DARWIN: towards the ultimate dark matter detector,” *JCAP* **11**, 017 (2016).
  - [11] J. Aalbers *et al.* (XLZD), “The XLZD Design Book: Towards the Next-Generation Dark Matter Observatory,” (2024).
  - [12] Johnathon R. Jordan, Sebastian Baum, Patrick Stengel, Alfredo Ferrari, Maria Cristina Morone, Paola Sala, and Joshua Spitz, “Measuring Changes in the Atmospheric Neutrino Rate Over Gigayear Timescales,” *Phys. Rev. Lett.* **125**, 231802 (2020), arXiv:2004.08394 [hep-ph].
  - [13] Natalia Tapia-Arellano and Shunsaku Horiuchi, “Measuring solar neutrinos over gigayear timescales with paleo detectors,” *Phys. Rev. D* **103**, 123016 (2021), arXiv:2102.01755 [hep-ph].
  - [14] Sebastian Baum, Francesco Capozzi, and Shunsaku Horiuchi, “Rocks, water, and noble liquids: Unfolding the flavor contents of supernova neutrinos,” *Phys. Rev. D* **106**, 123008 (2022), arXiv:2203.12696 [hep-ph].
  - [15] Lorenzo Caccianiga, Lorenzo Apollonio, Federico Maria Mariani, Paolo Magnani, Claudio Galelli, and Alessandro Ventre, “Sedimentary rocks from Mediterranean drought in the Messinian age as a probe of the past cosmic ray flux,” *Phys. Rev. D* **110**, L121301 (2024), arXiv:2405.04908 [astro-ph.HE].
  - [16] Claudio Galelli, Lorenzo Caccianiga, Lorenzo Apollonio, Paolo Magnani, and Vincent Breton, “A volcanic chronosequence as a time-resolved paleo-detector array to study the cosmic-ray flux in the late Pleistocene and Holocene,” *JCAP* **04**, 023 (2026), arXiv:2510.23126 [astro-ph.HE].
  - [17] S. Baum, T. D. P. Edwards, K. Freese, and P. Stengel, “New Projections for Dark Matter Searches with Paleo-Detectors,” *Instruments* **5**, 21 (2021), arXiv:2106.06559 [astro-ph.CO].
  - [18] A. Fung, T. Lucas, L. Balogh, M. Leybourne, and A. C. Vincent, “Refining the sensitivity of new physics searches with ancient minerals,” *Phys. Rev. D* **112**, 043040 (2025), arXiv:2504.08885 [hep-ph].
  - [19] B. K. Cogswell, A. Goel, and P. Huber, “Passive Low-Energy Nuclear-Recoil Detection with Color Centers,” *Phys. Rev. Applied* **16**, 064060 (2021), arXiv:2104.13926 [physics.ins-det].
  - [20] G. R. Araujo *et al.* (PALEOCCENE), “Nuclear recoil detection with color centers in bulk lithium fluoride,” (2025), arXiv:2503.20732 [physics.ins-det].
  - [21] N. Vladimirov *et al.*, “Benchtop mesoSPIM: a next-generation open-source light-sheet microscope for cleared samples,” *Nature Communications* (2024), 10.1038/s41467-024-46770-2.
  - [22] S. Chatrchyan *et al.* (CMS), “The CMS experiment at the CERN LHC,” *JINST* **3**, S08004 (2008).
  - [23] G. Aad *et al.* (ATLAS), “The ATLAS Experiment at the CERN Large Hadron Collider,” *JINST* **3**, S08003 (2008).
  - [24] J. F. Ziegler, M. D. Ziegler, and J. P. Biersack, “SRIM – The Stopping and Range of Ions in Matter (2010),” *Nucl. Instrum. Meth. B* **268**, 1818–1823 (2010).

- [25] S. Agarwal, Y. Lin, C. Li, R. E. Stoller, and S. J. Zinkle, “On the use of SRIM for computing radiation damage exposure,” *Nucl. Instrum. Meth. B* **503**, 11–29 (2021).
- [26] J. Billard, L. Strigari, and E. Figueroa-Feliciano, “Implication of neutrino backgrounds on the reach of next generation dark matter direct detection experiments,” *Phys. Rev. D* **89**, 023524 (2014), arXiv:1307.5458 [hep-ph].
- [27] Ciaran A. J. O’Hare, “New definition of the neutrino floor for direct dark matter searches,” *Phys. Rev. Lett.* **127**, 251802 (2021), arXiv:2109.03116 [hep-ph].
- [28] L Wang, W Gong, S Wang, and R C Ewing, “Comparison of ion-beam irradiation effects in xsub 2yosub 4 compounds,” *Journal of the American Ceramic Society* **82** (1999).
- [29] P. W. May, G. Pineau des Forêts, D. R. Flower, D. Field, N. L. Allan, and J. A. Purton, “Sputtering of grains in c-type shocks,” *Monthly Notices of the Royal Astronomical Society* **318**, 809–816 (2000), <https://academic.oup.com/mnras/article-pdf/318/3/809/3474381/318-3-809.pdf>.
- [30] Marco Bocchio, *Modelling Dust Processing and Evolution in Extreme Environments as seen by Herschel Space Observatory*, Ph.D. thesis, Institut d’Astrophysique Spatiale (2014).
- [31] Webmineral Mineralogy Database, “Olivine Mineral Data,” <https://webmineral.com/data/Olivine.shtml>, accessed: 2026-05-07.
- [32] J. Nahum and D. A. Wiegand, “Optical properties of some F-aggregate centers in LiF,” *Physical Review* **154**, 817–830 (1967).
- [33] G. Baldacchini, M. Cremona, G. d’Auria, R. M. Montereali, and V. Kalinov, “Optical bands of F<sub>2</sub> and F<sub>3</sub><sup>+</sup> color centers in LiF,” *Physical Review B* **54**, 17508–17516 (1996).
- [34] A. M. Zaitsev, *Optical Properties of Diamond: A Data Handbook* (Springer, Berlin, Heidelberg, 2001).
- [35] S. Castelletto and A. Boretti, “Silicon carbide color centers for quantum applications,” *Journal of Physics: Photonics* **2**, 022001 (2020).
- [36] R. H. Helm, “Inelastic and Elastic Scattering of 187-Mev Electrons from Selected Even-Even Nuclei,” *Phys. Rev.* **104**, 1466–1475 (1956).
- [37] J. D. Lewin and P. F. Smith, “Review of mathematics, numerical factors, and corrections for dark matter experiments based on elastic nuclear recoil,” *Astropart. Phys.* **6**, 87–112 (1996).
- [38] M. C. Smith *et al.*, “The RAVE Survey: Constraining the Local Galactic Escape Speed,” *Mon. Not. Roy. Astron. Soc.* **379**, 755–772 (2007), arXiv:astro-ph/0611671.
- [39] J. I. Read, “The Local Dark Matter Density,” *J. Phys. G* **41**, 063101 (2014), arXiv:1404.1938 [astro-ph.GA].
- [40] J. Aalbers *et al.* (LZ), “Dark Matter Search Results from 4.2 Tonne-Years of Exposure of the LUX-ZEPLIN (LZ) Experiment,” (2024), arXiv:2410.17036 [hep-ex].
- [41] A. Zabi *et al.*, “The CMS data acquisition system for the Phase-2 upgrade,” *Proceedings of Science (Topical Workshop on Electronics for Particle Physics 2018)* (2019), 10.22323/1.343.0129, arXiv:1806.08975.
- [42] Samuel Hedges, “Imaging nuclear recoil damage in minerals with light-sheet microscopy,” Talk presented at the MDνDM 2026 – Mineral Detection of Neutrinos and Dark Matter workshop Karlsruhe, Germany (2026).
- [43] A. Shapson-Coe *et al.*, “A petavoxel fragment of human cerebral cortex reconstructed at nanoscale resolution,” *Science* **384**, eadk4858 (2024).